SCIENCE CHINA
Earth Sciences

• RESEARCH PAPER •

November 2014 Vol.57 No.11: 2587–2596
doi: 10.1007/s11430-014-4840-5

A numerical study of the effect of the marginal sea on coastal upwelling in a non-linear inertial model

CHAO JiPing[2], KANG YanYan[1,3*] & LI JianPing[2]

[1] *LASG, Institute of Atmospheric Physics, Chinese Academy of Sciences, Beijing 100029, China;*
[2] *National Marine Environmental Forecasting Center, Beijing 100081, China;*
[3] *College of Earth Sciences, University of Chinese Academy of Sciences, Beijing 100049, China*

Received May 29, 2013; accepted December 4, 2013; published online September 12, 2014

Inertia theory and the finite element method are used to investigate the effect of marginal seas on coastal upwelling. In contrast to much previous research on wind-driven upwelling, this paper does not consider localized wind effects, but focuses instead on temperature stratification, the slope of the continental shelf, and the background flow field. Finite element method, which is both faster and more robust than finite difference method in solving problems with complex boundary conditions, was developed to solve the partial differential equations that govern coastal upwelling. Our results demonstrate that the environment of the marginal sea plays an important role in coastal upwelling. First, the background flow at the outer boundary is the main driving force of upwelling. As the background flow strengthens, the overall velocity of cross-shelf flow increases and the horizontal scale of the upwelling front widens, and this is accompanied by the movement of the upwelling front further offshore. Second, temperature stratification determines the direction of cross-shelf flows, with strong stratification favoring a narrow and intense upwelling zone. Third, the slope of the continental shelf plays an important role in controlling the intensity of upwelling and the height that upwelling may reach: the steeper the slope, the lower height of the upwelling. An additional phenomenon that should be noted is upwelling separation, which occurs even without a local wind force in the nonlinear model.

coastal upwelling, inertia theory, Finite Element Method (FEM)

Citation: Chao J P, Kang Y Y, Li J P. 2014. A numerical study of the effect of the marginal sea on coastal upwelling in a non-linear inertial model. Science China: Earth Sciences, 57: 2587−2596, doi: 10.1007/s11430-014-4840-5

Upwelling raises cold, nutrient-rich waters to the surface, which encourages seaweed growth and supports the bloom of phytoplankton. It plays a vital role in fishery production and determines the location of fishing grounds. Furthermore, the inner shelf region, because of the upwelling separation, acts as a barrier to cross-shelf transport, which enhances the retention of fish eggs and larvae within the coastal environment (Roy et al., 1998). Upwelling also plays an important role in the global carbon cycle (Anderson et al., 2009). Therefore, the intensity and location of upwelling is important to marine ecosystems, which has motivated decades of study on the dynamics of the upwelling process.

Previous research has mostly focused on wind-driven upwelling. However, there is also much research indicating that the local wind stress is not the main force driving the upwelling along some coasts. Zhao et al. (2003) reported that upwelling off the Yangtze River estuary is caused by interaction between the Taiwan Warm Current and the topography. Hu et al. (1980) suggested that upwelling off the Zhejiang coast was mainly a result of the rise of the Kuroshio Current along the bottom shoreward. Previous results also showed that coastal upwelling is highly correlated with the seasonal and annual variability of the Taiwan Warm

*Corresponding author (email: yanyan051022@163.com)

Current (Yan et al., 1992). Oke et al. (2000) indicated that coastal upwelling off eastern Australia is mainly caused by alongshelf topographic variations. Besides the wind and background current, the tide has been demonstrated to be a dominant driver of costal upwelling off the Yangtze River estuary and Zhejiang coast in China via barotropic and baroclinic processes (Huang et al., 1996; Lü et al., 2007). The present paper therefore discusses the effects of factors such as the background current, topography and stratification without a local wind force.

Present theory predicts that a steep continental shelf favors narrow and intense upwelling, while a gentle slope favors broad and weak upwelling. Allen et al. (1995) concluded that, over a wide shelf, onshore flow is confined to the bottom boundary layer and the upwelling front is weak; while over a steep shelf, the onshore flow occurs primarily through the interior, and the upwelling front is stronger, and near the coast. Bakun (1996) found that upwelling separation may not occur in the absence of a steep slope. Estrade et al. (2008) demonstrated that, in the case of an alongshore wind, the cross-shore width of upwelling scaled with D/S, where D is the thickness of Ekman layer, S is the bottom topographic slope. Peffley et al. (1976) and Rodrigues et al. (2001) studied the effects of the bottom topography and the coastline on wind-driven upwelling off the Oregon coast and Brazilian coast. The relative importance of topography and coastline depends on the specific sea; where the coastline is straight, the topography contributes more to the driving of upwelling. Gan et al. (2009a) showed that the alongshore variation of bottom topography caused the upwelling center in Regional Ocean Model System (ROMS), that the upwelling intensified over a widened shelf between Shantou and Shanwei, and there were upwelling centers in Shantou. The previous studies show that bottom topography plays an important role in coastal upwelling.

Stratification also greatly affects coastal upwelling. Allen et al. (1995) found that, with reduced temperature stratification, the coastal upwelling and along-shore jet stream weakened, and the front was farther offshore. In the stratified case, a major part of the upwelling cell was within 3 km of the coast, while in a homogeneous experiment, the upwelling cell was located 8 km offshore. Austin et al. (2002) reported similar results showing that cross-shore transport reduced as stratification weakened. Lentz (2001) reported that there was a marked difference in cross-shelf transport between summer, when waters were more stratified, and fall, when waters were weakly stratified. Kirincich (2005) simulated the separation of upwelling as stratification weakens. Gan et al. (2009b) pointed out that cross-shore circulation strengthens at a higher level of stratification by a plume. Additionally, recent research has suggested that upwelling has intensified off northwest Africa and in the northern South China Sea (NSCS) as the planet has warmed (Liu et al., 2009; McGregor et al., 2007).

Most of the previous work is based on numerical models, whereas little has been done on the basic theory of upwelling. The numerical simulations always depend heavily on parameterization of the turbulent mixing and momentum, and therefore it is difficult to explain the physical mechanism. In this paper, we examine non-wind-driven upwelling with nonlinear inertia theory. The inertia theory was first used for the Gulf Stream by Charney (1955), and Pedlosky (1978) then applied the inertia theory to coastal upwelling in predicting velocity and density fields. The nonlinear inertia model used in the present paper is derived from the inertia model of Chao et al. (2003), who used the model to obtain the coastal jet and temperature front. In contrast to Chao's theory, this study considers a non-linear temperature stratification and different bottom topography, and uses the finite element method (FEM) to solve the governing equation. Three experiments are conducted to investigate the effects of stratification, background circulation and topography.

1 Model equations

A left-handed "west coast" coordinate system is used, with positive x being the offshore direction, positive y the northward direction, and positive z the upward direction. The x–z dimensional equations eliminating along-shelf variability are

$$u\frac{\partial u}{\partial x}+w\frac{\partial u}{\partial z}-fv=-\frac{1}{\rho_0}\frac{\partial p}{\partial x}, \tag{1}$$

$$u\frac{\partial v}{\partial x}+w\frac{\partial v}{\partial z}+fu=0, \tag{2}$$

$$u\frac{\partial w}{\partial x}+w\frac{\partial w}{\partial z}=-\frac{1}{\rho_0}\frac{\partial p}{\partial z}-(1-\alpha T)\mathrm{g}, \tag{3}$$

$$u\frac{\partial T}{\partial y}+w\frac{\partial T}{\partial z}=0, \tag{4}$$

$$\frac{\partial u}{\partial x}+\frac{\partial w}{\partial z}=0, \tag{5}$$

where α is the coefficient of the thermal expansion of the seawater, and the other symbols are those commonly used in the literature.

A stream function is introduced according to continuity eq. (5):

$$u=-\frac{\partial \psi}{\partial z},\ w=\frac{\partial \psi}{\partial x}. \tag{6}$$

Equations (2) and (4) then take the form

$$J(\psi,\ v+fx)=0, \tag{7}$$

$$J(\psi,\ T)=0, \tag{8}$$

and it follows that

$$v + fx = F_1(\psi), \tag{9}$$

$$T = F_2(\psi), \tag{10}$$

where $F_i(\psi)$ is an arbitrary function of ψ to be determined. To evaluate $F_i(\psi)$, we introduce cross-shore velocity u_∞ for the outer boundary condition ($x = \infty$). Eq. (6) then gives z as a function of ψ_∞, $z = -\psi_\infty / u_\infty$. In addition, we assume $v_\infty = v_0 + \Lambda z$ and $T_\infty = T_0 + \Gamma_1 z + \Gamma_2 z^2 + \Gamma_3 z^3$ for the outer boundary condition. Differentiating eq. (9), we have

$$\frac{\partial v_\infty}{\partial z} = \frac{\partial F_1(\psi_\infty)}{\partial \psi_\infty}\frac{\partial \psi_\infty}{\partial z} = \Lambda,$$

so that

$$\frac{\mathrm{d}F_1}{\mathrm{d}\psi_\infty} = -\frac{\Lambda}{\mu_\infty}. \tag{11}$$

In the same way,

$$\frac{\mathrm{d}F_2}{\mathrm{d}\psi_\infty} = -\frac{\Gamma_1 + 2\Gamma_2 z + 3\Gamma_3 z^2}{\mu_\infty} = -\frac{\Gamma_1}{\mu_\infty} + 2\frac{\Gamma_2}{\mu_\infty^2}\psi_\infty - 3\frac{\Gamma_3}{\mu_\infty^3}\psi_\infty^2. \tag{12}$$

Eliminating p from eqs. (1) and (3), we have

$$u\frac{\partial}{\partial x}\left(\frac{\partial u}{\partial z} - \frac{\partial w}{\partial x}\right) + w\frac{\partial}{\partial z}\left(\frac{\partial u}{\partial z} - \frac{\partial w}{\partial x}\right) - f\frac{\partial v}{\partial z} + \mathrm{g}\alpha\frac{\partial T}{\partial x} = 0. \tag{13}$$

Using eqs. (11) and (12), eq. (13) can be written as

$$\vec{U}\cdot\left(\frac{\partial^2\psi}{\partial x^2} + \frac{\partial^2\psi}{\partial z^2} - f\frac{\mathrm{d}F_1}{\mathrm{d}\psi} - \mathrm{g}\alpha\frac{\mathrm{d}F_2}{\mathrm{d}\psi}\right) = 0, \tag{14}$$

or

$$\frac{\partial^2\psi}{\partial x^2} + \frac{\partial^2\psi}{\partial z^2} - f\frac{\mathrm{d}F_1}{\mathrm{d}\psi} - \mathrm{g}\alpha\frac{\mathrm{d}F_2}{\mathrm{d}\psi} = F_3(\psi). \tag{15}$$

Using eqs. (11) and (12), eq. (15) can be written as

$$\frac{\partial^2\psi}{\partial x^2} + \frac{\partial^2\psi}{\partial z^2} + \frac{f\Lambda}{\mu_\infty}x - \mathrm{g}\alpha\left(-\frac{\Gamma_1}{\mu_\infty} + 2\frac{\Gamma_2}{\mu_\infty^2}\psi_\infty - 3\frac{\Gamma_3}{\mu_\infty^3}\psi_\infty^2\right)z = F_3(\psi). \tag{16}$$

Along the outer boundary,

$$F_3(\psi_\infty) = \frac{f\Lambda}{\mu_\infty}x_\infty + \mathrm{g}\alpha\frac{\psi_\infty}{\mu_\infty}\left(-\frac{\Gamma_1}{\mu_\infty} + \frac{2\Gamma_2\psi_\infty}{\mu_\infty^2} - \frac{3\Gamma_3\psi_\infty^2}{\mu_\infty^3}\right), \tag{17}$$

where x_∞ is the width of the inertia domain, or the offshore distance of the outer boundary. F_1, F_2, F_3 are determined along the outer boundary and are consequently applicable to every point in the interior region. We then have the governing equation:

$$\frac{\partial^2\psi}{\partial x^2} + \frac{\partial^2\psi}{\partial z^2} - \mathrm{g}\alpha\left(-\frac{\Gamma_1}{\mu_\infty^2} + 2\frac{\Gamma_2}{\mu_\infty^3}\psi - 3\frac{\Gamma_3}{\mu_\infty^4}\psi^2 + 2\frac{\Gamma_2}{\mu_\infty^2}z - 3\frac{\Gamma_3}{\mu_\infty^3}\psi z\right)\psi = -\frac{f\Lambda}{\mu_\infty}(x - x_\infty) - \mathrm{g}\alpha\frac{\Gamma_1}{\mu_\infty}z. \tag{18}$$

The nonlinear partial differential equations have been converted into a second-order elliptic equation of a single variable. In the equation, f=0.9×10^{-4} s^{-1}, g=9.8 m s^{-2}, α= 1.8×10^{-4} °C^{-1}, the vertical along-shore velocity gradient Λ= 0.003 s^{-1}, and the bottom topography is taken to be $h_c(x)$= $h_0\exp(-\beta(x/100)^2)$, where h_0=195 m, β=3.4×10^{-6} m^{-2}. The stratification parameters are given according to the measured temperature in the NSCS.

The boundary conditions for $\psi(x, z)$ are

$$\begin{aligned}&\psi(x,0) = 0,\\ &\psi(x,h_c(x)) = 0,\\ &\psi(0,z) = 0,\\ &\frac{\partial\psi}{\partial x}(x_\infty, z) = 0.\end{aligned} \tag{19}$$

2 Numerical method

To handle the computational complexity of the terrain, the FEM is used here to solve the nonlinear elliptical eq. (18). In contrast to the finite difference method widely used in previous papers, the FEM is fast and robust in solving a problem with complex boundary conditions.

2.1 Calekin method (weighted residual method)

The Calekin method is also known as a "weighted residual method". The idea is to satisfy the differential equation in an average sense by converting it into an integral equation. The differential equation is multiplied by a weighting function and then averaged over the domain.

The governing eq. (18) can be simplified as

$$\frac{\partial^2\psi}{\partial x^2} + \frac{\partial^2\psi}{\partial z^2} - a(\psi)\psi = F(x,z), \tag{20}$$

with the boundary conditions

$$\Gamma_1:\ \psi = \psi_0,\ \psi_0 \text{ is a constant},$$

$$\Gamma_2:\ \frac{\partial\psi}{\partial n} = \mathrm{G},\ \mathrm{G} \text{ is a constant},$$

where

$$a(\psi) = \mathrm{g}\alpha\left(-\frac{\Gamma_1}{\mu_\infty^2} + 2\frac{\Gamma_2}{\mu_\infty^3}\psi - 3\frac{\Gamma_3}{\mu_\infty^4}\psi^2 + 2\frac{\Gamma_2}{\mu_\infty^2}z - 3\frac{\Gamma_3}{\mu_\infty^3}\psi z\right)$$

and $f(x,z)=-\dfrac{f\Lambda}{\mu_\infty}(x-\xi)-\mathrm{g}\alpha\dfrac{\Gamma_1}{\mu_\infty}z$.

To solve eq. (20), we set

$$R=\frac{\partial^2\psi}{\partial x^2}+\frac{\partial^2\psi}{\partial z^2}-a(\psi)\psi-f(x,z), \tag{21}$$

where R is called the residual. Hence, solving eq. (20) is equivalent to calculating the weak form of $R(\psi)=0$,

$$\langle R,N\rangle=\int_s N^{\mathrm{T}}\left(\frac{\partial^2\psi}{\partial x^2}+\frac{\partial^2\psi}{\partial z^2}-a(\psi)\psi-f(x,z)\right)\mathrm{d}x\mathrm{d}z, \tag{22}$$

where $\psi=(N\psi)=N_1\psi_1+N_2\psi_2+\ldots+N_n\psi_n$, N is a shape function and n is the total number of nodes.

After introducing the boundary conditions into eq. (22), we have

$$\rho(\psi)=\langle R,N\rangle$$
$$=\int_s N^{\mathrm{T}}\left(\frac{\partial^2(N\psi)}{\partial x^2}+\frac{\partial^2(N\psi)}{\partial z^2}-a\big((N\psi)\big)(N\psi)-f(x,z)-\mathrm{g}\right)\cdot\mathrm{d}x\mathrm{d}z. \tag{23}$$

Equation (23) can be rearranged and solved using the Newton-Raphson method. We start the process with an initial guess $\psi^{(n)}$, and set $\psi^{(n+1)}$ to satisfy $\rho(\psi^{(n+1)})=0$, then

$$\frac{\partial\rho(\psi^n)}{\partial\psi}(\psi^{n+1}-\psi^n)=\rho(\psi^{(n+1)})-\rho(\psi^n)=-\rho(\psi^n), \tag{24}$$

$$W=\psi^{n+1}-\psi^n=\frac{-\rho(\psi^n)}{\dfrac{\partial\rho(\psi^n)}{\partial\psi}}. \tag{25}$$

The process is repeated until a sufficiently accurate value is reached.

2.2 Element type: Eight-node quadrangular element

Usually, a quadrangular element provides higher accuarcy than a triangular element. To increase the computational accuracy, an eight-node quadrangular element with second-order Lagrangian interpolation is used in the simulation. The Lagrangian interpolation can be expressed as

$$\psi^e(\varepsilon,\eta)=a_1+a_2\varepsilon+a_3\eta+a_4\varepsilon^2+a_5\varepsilon\eta+a_6\eta^2+a_7\varepsilon^2\eta+a_8\varepsilon\eta^2. \tag{26}$$

To check the accuracy of our FEM code, we solved the nonlinear Ginzburg-Landau equation (eq. (27)) using our FEM code and compared the results with those obtained by Alberty et al. (1999) using a four-node quadrilateral element (Figure 1):

$$\varepsilon\Delta\psi=\psi^3-\psi,\ \psi=0 \text{ on } \Gamma, \text{ where } \varepsilon=1/100. \tag{27}$$

3 Observation

We consider the case of the NSCS to determine the parameters associated with stratification. Figure 2 shows the temperature profile from 0 to 200 m below the surface of the NSCS in July. Because of the limited data resolution, the bottom topography cannot be seen clearly, especially in the Taiwan Strait where the depth is less than 40 m and there is only one layer. However, we are still able to identify the low-temperature region near the shore, and this suggests the existence of upwelling as indicated by the arrow.

Taking 19.5°N as an example, the longitude-depth cross-section of temperature between January and December is shown in Figure 3. It is clear that the highest sea surface temperature occurred in July, and the lowest in January, so that the stratification is strongest in July and weakest in January. To examine the effect of stratification on upwelling, we used the observed stratification from July, September, November and January (stratifications 1, 2, 3, and 4, respectively, in Figure 4) in the following simulations. Data used in this study are from the CORA National Marine Information Center (http://www.cora.net.cn/).

4 Simulation results

4.1 Effects of stratification

Our results are for a depth of 200 m, offshore distance of 130 km, and $u_\infty=-0.06\ \mathrm{m\ s^{-1}}$. Figure 5 shows that coastal upwelling occurred in stratification cases 1–4. With the lower sea surface temperatures, stratification is reduced, upwelling weakens, and the width of the upwelling increases. Hence, strong temperature stratification favors strong and narrow

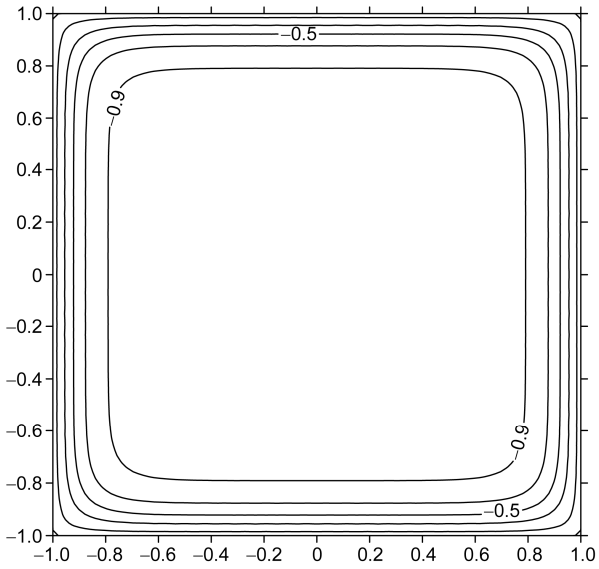

Figure 1 Solution for the Ginzburg-Landau equation.

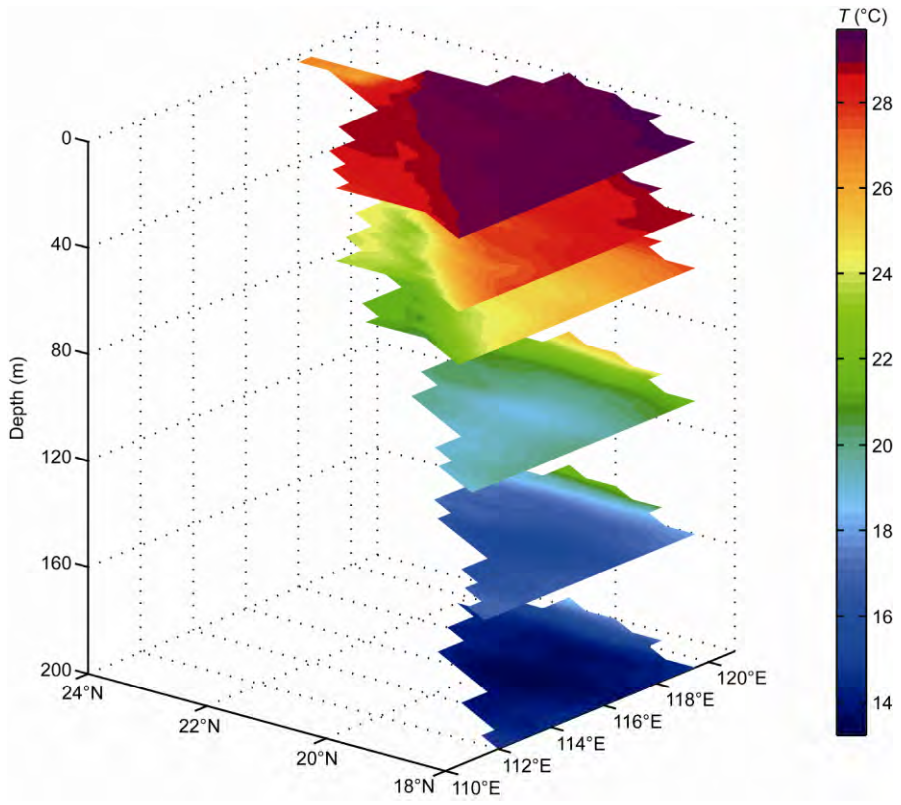

Figure 2 Temperature slice (from 0 to 200 m below the sea surface) of the NSCS in July.

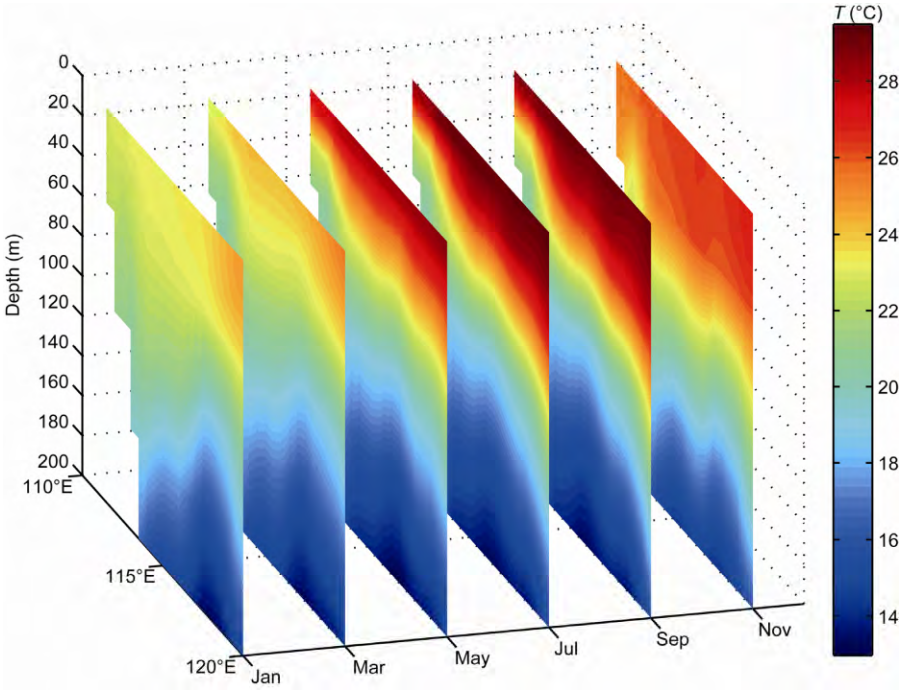

Figure 3 Longitude-depth cross-section of temperature from January to December at 19.5°N.

upwelling. However, in the case of stratification 4, during winter, there is downwelling. In all four temperature stratification scenarios, the inflow and outflow were confined to the bottom and surface boundary layers, respectively. Another important phenomenon, termed upwelling separation, is a zone of increased vertical velocity that developed 12 km from the coast, which was not reported by Chao et al. (2003). To confirm that this upwelling separation is not

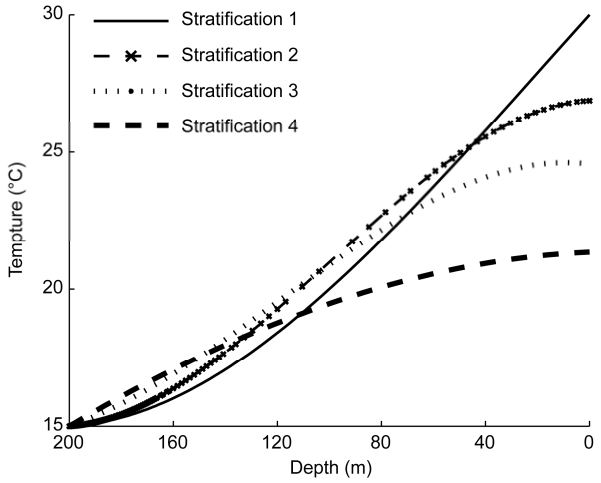

Figure 4 Four stratification scenarios used in simulations.

caused by the FEM code, we solved Chao's linear equation using the FEM code. We found that the results are consistent with Chao's linear model (Figure 6). We therefore conclude that upwelling separation is caused by the nonlinear field accelerations associated with the nonlinear temperature stratification. The inner shelf is the region inshore of the upwelling front (Austin, 2002). In Figure 5(a)–(d) correspond to stratification scenarios 1–4, respectively, and it is seen that the width of the inner shelf does not vary with the stratification.

4.2 Effects of u_∞

The effects of u_∞ are examined using the same terrain and stratification as used in experiment 1, and by increasing u_∞

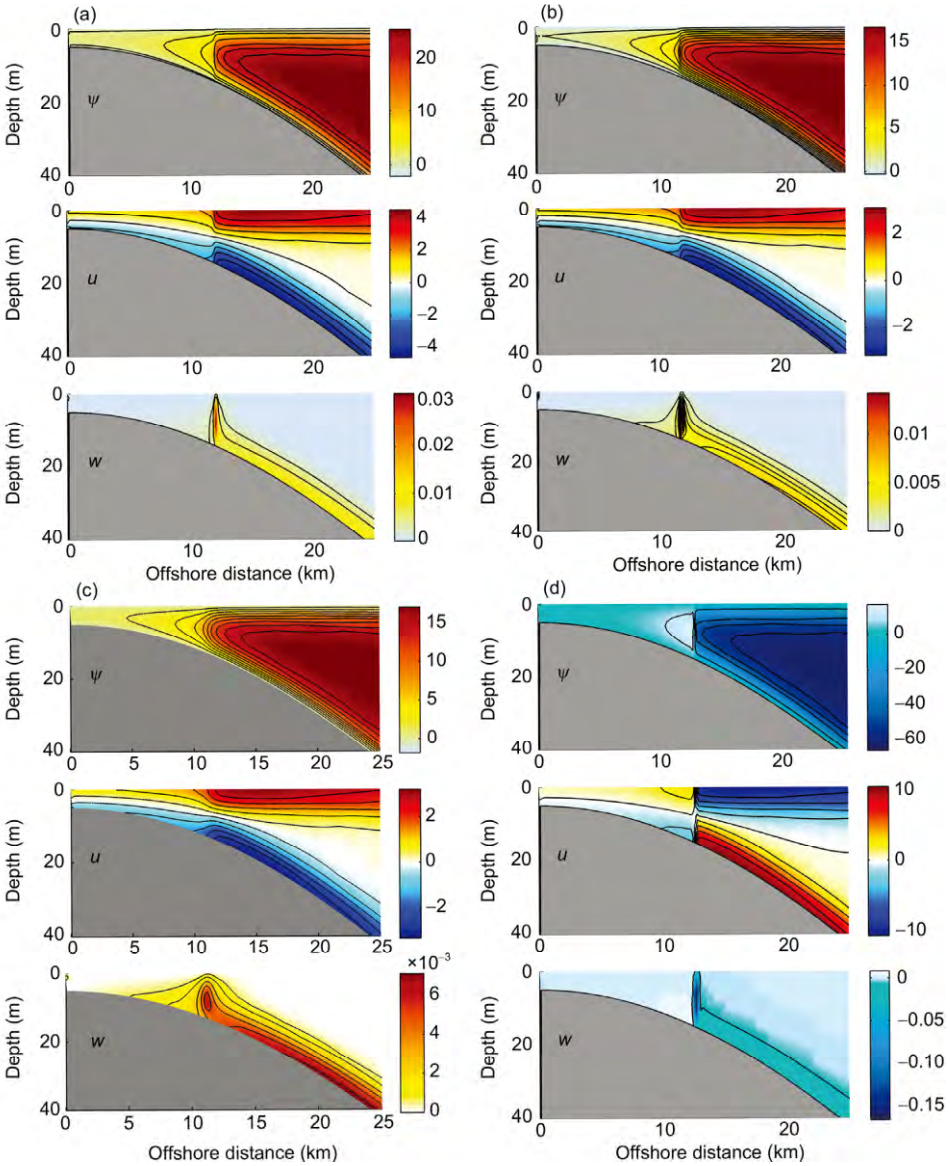

Figure 5 Streamfunction, cross-shelf velocity and vertical velocity fields for u_∞ =–0.06 m s^{-1}. (a)–(d) correspond to stratifications 1–4 respectively. The units of u and w are m s^{-1}.

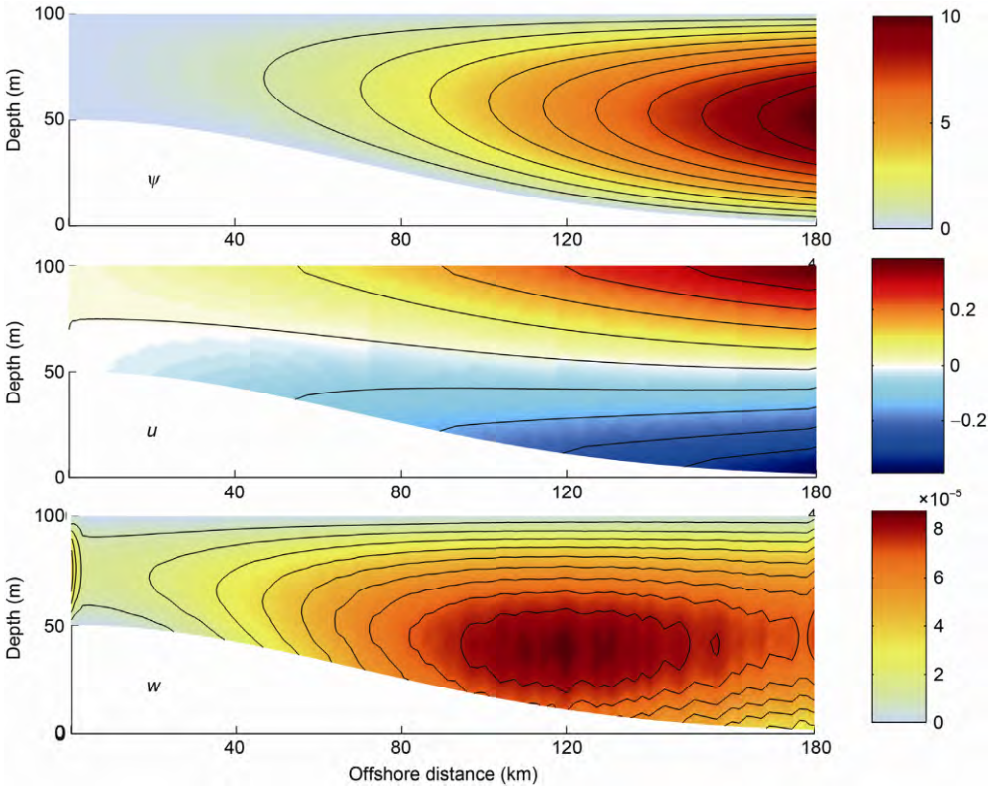

Figure 6 Streamfunction, cross-shelf velocity and vertical velocity fields been obtained with the FEM. The units of u and w are m s^{-1}

from –0.06 to –0.3 m s^{-1} (Figure 7). The flow pattern does not change, and upwelling still occurs in July, September, and November, and downwelling in January. However, the intensity and horizontal scale of the upwelling front increases, and the boundary layer thickens. The second distinctive feature is that the offshore distance of the upwelling front increases from 12 km when u_∞=–0.06 m s^{-1} to 35 km when u_∞=–0.3 m s^{-1}.

A further experiment considered the effect of gradually increasing u_∞ from –0.06 to –0.3 m s^{-1} under the conditions of stratification scenario 2. We see that the offshore distance and the width of the inner shelf increase from 12 to about 60 km (Figure 8). Because fish tend to avoid spawning in the vicinity of upwelling centers (Roy et al., 1998), the widened inner shelf would notably affect the nearshore ecosystem.

4.3 Effect of topography

To examine the role played by topography, a steep, narrow continental shelf is used in the following simulation. Compared with experiment 1, the water depth remains at 200 m and u_∞=–0.06 m s^{-1}, but the offshore distance decreases to 13 km. The results (Figure 9) show that the flow pattern does not change under stratification scenarios 1 and 4, although the intensity is enhanced. However, in the cases of stratification scenarios 2 and 3, the flow pattern changes dramatically, in that the upwelling cannot reach the sea surface and the return flow is in the interior. Xu et al. (1983) and Pan et al. (1982) pointed out that the upwelling cell off the Zhejiang coast mainly exists 5 m below the sea surface, and it reaches the sea surface only in certain months. However, they did not discuss what factors may affect the height that the upwelling can reach. Additionally, Su et al. (2009) and Dong et al. (2004) found two counterrotating cells in the vertical direction using an analytical model. MacCready et al. (1993) indicated that the location of the return flow depends on the relative importance of stratification and topography for wind-driven upwelling (Austin et al., 2002; MacCready et al., 1993). The location of the offshore flow in our study also depends on the topography, even though it is not driven by local wind.

To further examine the effect of the continental slope on the location of the offshore flow, we increase the continental shelf slope by shortening the offshore distance to 42, 39, 26, and then 13 km, with water depth remaining the same, u_∞=–0.06 m s^{-1}, and using stratification scenario 2. It is fairly clear that the height that the upwelling can reach is reduced over the deeper continental shelf, and that the upwelling cannot reach the ocean surface when the offshore distance is less than 42 km (Table 1). That is, a wider shelf favors a surface offshore flow, while a steeper continental shelf favors an interior offshore flow. Gan et al. (2009a) has

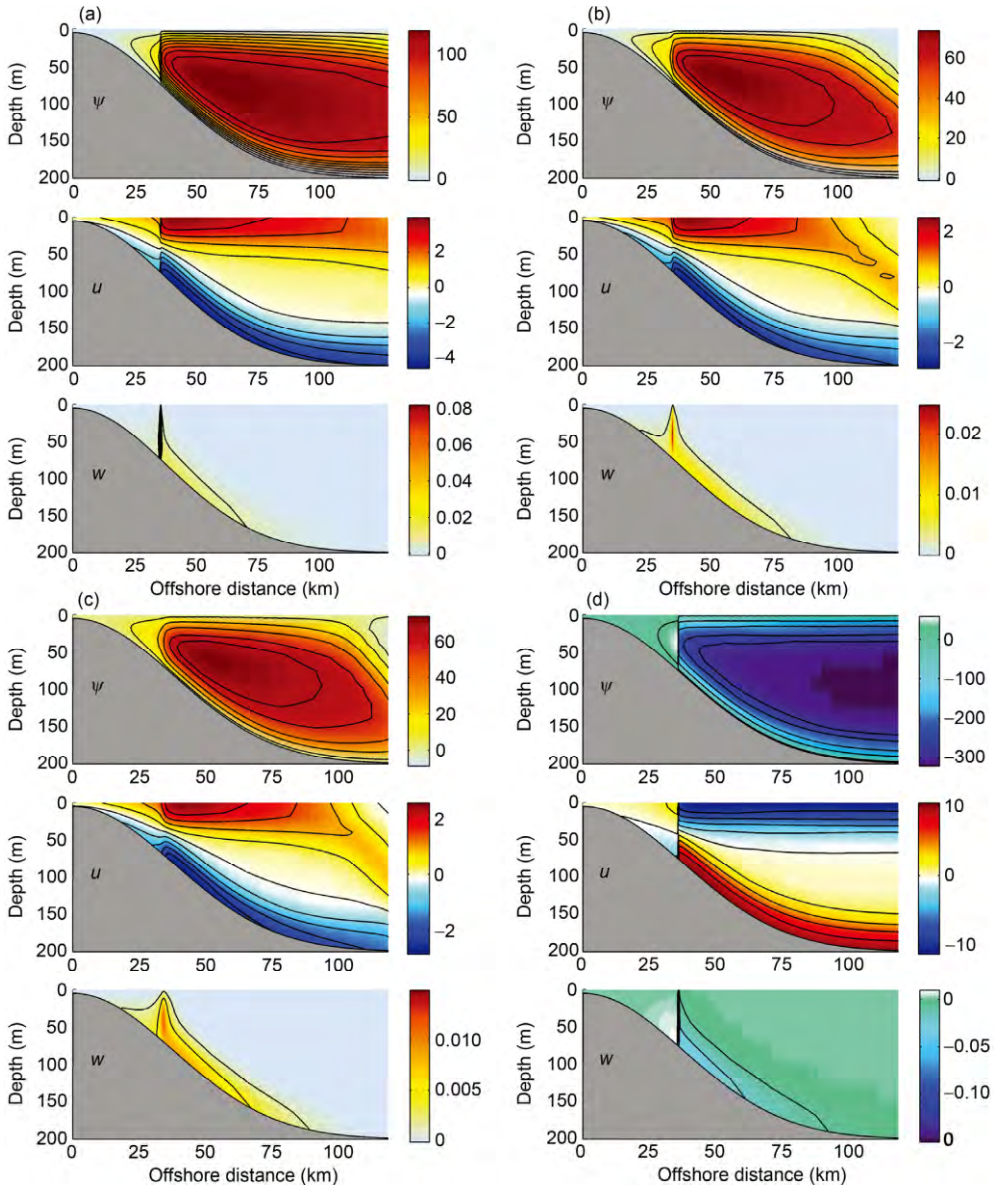

Figure 7 Streamfunction, cross-shelf velocity and vertical velocity fields for u_∞ =–0.3 m s^{-1}. (a)–(d) correspond to stratifications 1–4 respectively. The units of u and w are m s^{-1}.

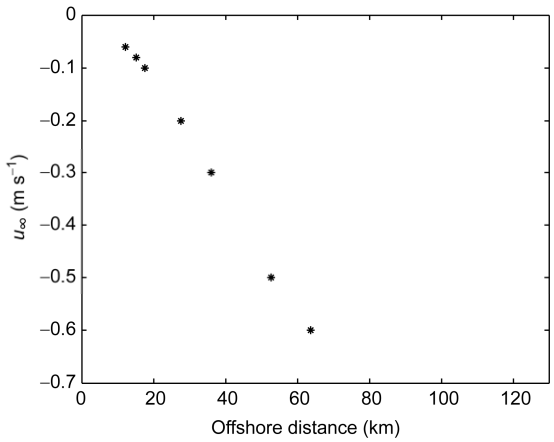

Figure 8 Offshore distance of separation point as a function of u_∞.

also pointed out that upwelling strengthened over a widened shelf between Shantou and Shanwei.

5 Discussion and conclusion

The simple nonlinear model presented in this paper successfully reproduced the structure of coastal upwelling that is not driven by wind effects. Compared with Chao's linear model (Chao et al., 2003), we successfully simulated boundary-concentrated upwelling and the phenomenon of upwelling separation.

Strong stratification tends to generate strong and narrow upwelling, but with reduced stratification, upwelling weakens and the horizontal scale increases. Consequently, during

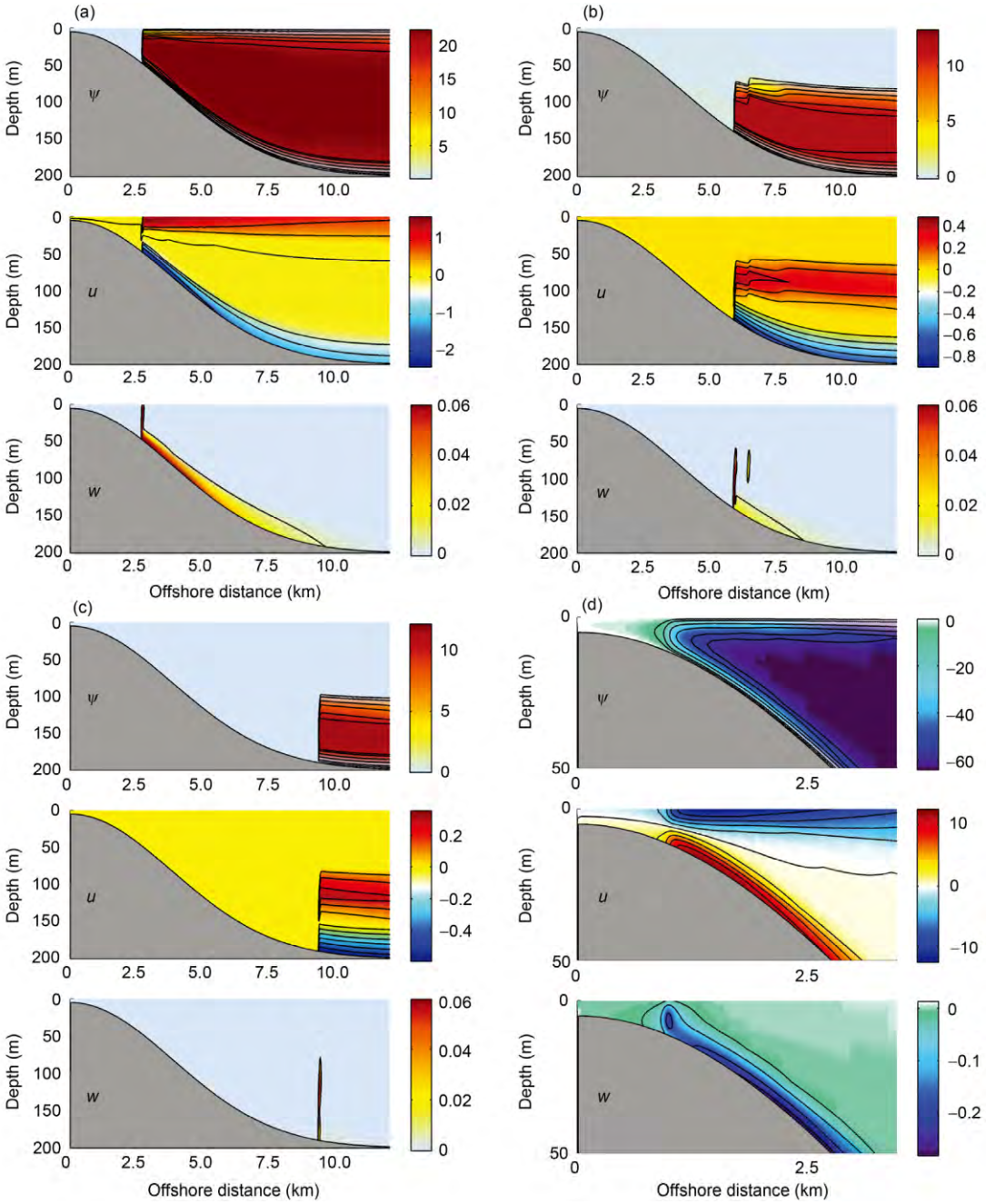

Figure 9 Streamfunction, cross-shelf velocity and vertical velocity fields over the deeper continental shelf (depth of 200 m, offshore distance of 13 km) for u_∞ =–0.06 m s^{-1}. (a)–(d) correspond to stratifications 1–4 respectively. The units of u and w are m s^{-1}.

Table 1 Height that upwelling can reach lowers over the deeper continental shelf

Offshore distance (km)	42	39	26	13
The height that upwelling can reach (m)	0	10	50	90

summer, the coastal upwelling front is strong and narrow, while in winter, when temperature stratification is weakest, downwelling may occur. In addition, the width of the inner shelf does not vary with the stratification. The well-known mechanism of upwelling separation is caused by the overlap of the surface and bottom Ekman layers, and reduces cross-shore transport. Kirincich (2005) and Estrade et al. (2008) showed that cross-shelf transport decreased, and upwelling separated, during periods of reduced stratification. Additionally, Estrade et al. (2008) found that the separation point was located near the isobath $h \approx 0.4D$, where D is the thickness of the Ekman layer. Nevertheless, the assumption made in this paper is of no-viscosity (i.e., no Ekman layer),

and instead we used the inertia boundary layer theory, which was first proposed by Charney (1955). Charney defined the inertia boundary layer as the region in which the nonlinear field accelerations are comparable in magnitude to the Coriolis and pressure forces per unit mass. The cross-shore velocity in the inertia boundary layer is much higher than that in the internal ocean. Hydrodynamic jump occurs during the transition from fast to slow fluid movement. In technical terms, the phenomenon occurs when the movement of water changes from being supercritical to being subcritical, which is observed when a fluid with a high critical mass meets a fluid with lower critical mass. The jump is determined by the Froude number (defined as $\sqrt{\frac{u^2}{gH}}$, where u is the cross-shore velocity, H is the water depth, and g is acceleration due to gravity). Therefore, the width of the inner shelf in inertia theory is related to the cross-shore velocity and bottom topography.

With increasing u_∞, the intensity and horizontal scale of the upwelling front increase, the inertia boundary thickens, and the separating point moves further offshore, leading to widening of the inner shelf. According to previous research on wind-driven upwelling, this widening of the inner shelf is caused by the thickening of the boundary layer. Under inertial theory, the boundary layer is related to u_∞ (i.e., increasing u_∞ results in a thicker boundary layer), which leads to an increase in the width of the inner shelf.

The response of upwelling to the topography depends on stratification. Over a steep continental shelf, the flow cannot reach the sea surface, and the height that the upwelling can attain decreases as the continental shelf steepens. However, during winter, there is always downwelling. The inertial model does not allow us to conclude any turbulent mixing coefficient or linearization hypothesis, and it thus cannot describe the mixing process. This would be better addressed if we consider a two-layer model in which the upper layer is the Ekman layer and the lower layer is the inertial layer. Another deficiency of this study is its inability to examine the effect of alongshore topography. Our future work will include a three-dimensional finite element model and two-layer model.

The study was supported by the National Basic Research Program of China (Grant No. 2010CB950400) and the program in National Marine Environmental Forecasting Center. The CORA data used in this study have been developed and kindly provided by National Marine Data. We greatly appreciate assistance and valuable suggestions provided Dr. Li Yaokun. We also thank two anonymous reviewers for their helpful advice and comments.

Alberty J, Carstensen C, Funken S A. 1999. Remarks around 50 lines of Matlab: Short finite element implementation. Numer Algorithms, 20: 117–137

Allen J, Newberger P, Federiuk J. 1995. Upwlling circulation on the oregon continental shelf. Part I: Response to idealized forcing. J Phys Oceanogr, 25: 1843–1866

Anderson R, Ali S, Bradtmiller L, et al. 2009. Wind-driven upwelling in the Southern Ocean and the deglacial rise in atmospheric CO_2. Science, 323: 1443

Austin J A, Lentz S J. 2002. The inner shelf response to wind-driven upwelling and downwelling. J Phys Oceanogr, 32: 2171–2193

Bakun A. 1996. Patterns in the Ocean: Ocean Processes and Marine Population Dynamics. California: California University Press. 323

Chao J P, Chen X Y. 2003. A semi-analytical theory of coastal upwelling and jet (in Chinese). Chin J Geophys, 46: 26–30

Charney J G. 1955. The Gulf Stream as an inertial boundary layer. Proc Natl Acad Sci USA, 41: 731

Dong C, Ou H W, Chen D, et al. 2004. Tidally induced cross-frontal mean circulation: Analytical study. J Phys Oceanogr, 34: 293–305

Estrade P, Marchesiello P, De Verdiere A C, et al. 2008. Cross-shelf structure of coastal upwelling: A two dimensional extension of Ekman's theory and a mechanism for inner shelf upwelling shut down. J Mar Res, 66: 589–616

Gan J P, Cheung A, Guo X, et al. 2009a. Intensified upwelling over a widened shelf in the northeastern South China Sea. J Geophys Res, 114: C09109

Gan J P, Li L, Wang D X, et al. 2009b. Interaction of a river plume with coastal upwelling in the northeastern South China Sea. Cont Shelf Res, 29: 728–740

Hu D X, Lü L H, Xiong Q C, et al. 1980. Study on the upwelling of Zhejiang coastal waters (in Chinese). Chin Sci Bull, 25: 131–133

Huang Z K, Yu G Y, Luo Y Y, et al. 1996. Numerical modeling of tide-induced upwelling in coastal areas of the East China Sea (in Chinese). J Ocean Univ Qingdao (Nat Sci Ed), 26: 405–412

Kirincich A R. 2005. Wind-driven inner-shelf circulation off central Oregon during summer. J Geophys Res, 110: C10S03

Lentz S J. 2001. The influence of stratification on the wind-driven cross-shelf circulation over the North Carolina Shelf. J Phys Oceanogr, 31: 2749–2760

Liu Y, Peng Z C, Wei G J, et al. 2009. Variation of summer coastal upwelling at northern South China Sea during the last 100 years. Geochimica, 38: 317–322

Lü X G, Qiao F L, Xia C S, et al. 2007. Tidally induced upwelling off Yangtze River estuary and in Zhejiang coastal waters in summer. Sci China Ser D-Earth Sci, 50: 462–473

MacCready P, Rhines P B. 1993. Slippery bottom boundary layers on a slope. J Phys Oceanogr, 23: 5–22

McGregor H, Dima M, Fischer H, et al. 2007. Rapid 20th-century increase in coastal upwelling off northwest Africa. Science, 315: 637

Oke P R, Middleton J H. 2000. Topographically induced upwelling off Eastern Australia. J Phys Oceanogr, 30: 512–531

Pan Y Q, Cao X Z, Xu J P. 1982. A preliminary investigation of the cause and characteristics of the upwelling front zone off Zhejiang (in Chinese). Trans Oceanol Limnol, 3: 1–7

Pedlosky J. 1978. An inertial model of steady coastal upwelling. J Phys Oceanogr, 8: 171–177

Peffley M B, O'Brien J J. 1976. A three-dimensional simulation of coastal upwelling off Oregon. J Phys Oceanogr, 6: 164–180

Roy C. 1998. An upwelling-induced retention area off Senegal: A mechanism to link pwelling and retention processes. S Afr J Marine Sci, 19: 89–98

Rodrigues R R, Lorenzzetti J A. 2001. A numerical study of the effects of bottom topography and coastline geometry on the Southeast Brazilian coastal upwelling. Cont Shelf Res, 21: 371–394

Su J, Pohlmann T. 2009. Wind and topography influence on an upwelling system at the eastern Hainan coast. J Phys Oceanogr, 114: C06017

Xu J P, Cao X Z, Pan Y Q. 1983. Evidence for the coastal upwelling off Zhejiang (in Chinese). Trans Oceanol Limnol, 4: 17–25

Yan T Z. 1992. Mechanism analysis of the coastal upwelling off Zhejiang and Qiongdong (in Chinese). Acta Oceanol Sin, 14: 12–18

Zhao B, Li H, Yang Y. 2003. Numerical simulation of upwelling in the Changjiang river mouth area (in Chinese). Studia Marina Sin, 45: 64–76